Shear jamming, discontinuous shear thickening, and fragile states in dry granular materials under oscillatory shear

Michio Otsuki[1,*] and Hisao Hayakawa[2]

[1]*Graduate School of Engineering Science, Osaka University, Toyonaka, Osaka 560-8531, Japan*
[2]*Yukawa Institute for Theoretical Physics, Kyoto University, Kitashirakawaoiwake-cho, Sakyo-ku, Kyoto 606-8502, Japan*

We numerically study the linear response of two-dimensional frictional granular materials under oscillatory shear. The storage modulus G' and the loss modulus G'' in the zero strain rate limit depend on the initial strain amplitude of the oscillatory shear before measurement. The shear jammed state (satisfying $G' > 0$) can be observed at an amplitude greater than a critical initial strain amplitude. The fragile state is defined by the emergence of liquid-like and solid-like states depending on the form of the initial shear. In this state, the observed G' after the reduction of the strain amplitude depends on the phase of the external shear strain. The loss modulus G'' exhibits a discontinuous jump corresponding to discontinuous shear thickening in the fragile state.

I. INTRODUCTION

Amorphous disordered materials such as granular media, colloidal suspensions, foams, and emulsions interact via dissipative and repulsive forces, and in a dense regime these systems can form solid-like jammed states. Liu and Nagel proposed a phenomenological phase diagram for jamming transition, in which a particulate system jams upon compression; however, it unjams upon application of a shear force [1]. This proposal attracted much attention among physicists [2,3]. The existence of jammed states have been verified in several numerical simulations of frictionless granular particles. In these works, a continuous change of pressure as well as a discontinuous change of the coordination number has been observed across the jamming transition density [4–6]. Other researchers have reported various critical scaling laws of rheological quantities near the jamming density for frictionless particles up to the present time under steady shear [7–30] and oscillatory shear [31,32].

In reality due to the roughness of particles, mutual friction between particles is unavoidable in granular systems. Bi *et al.* [33] suggested that the jamming process qualitatively differs between frictional and frictionless grains; in frictional systems, shear forces counterintuitively induces jammed states even below the friction-dependent critical fraction ϕ_{iso}. Such transition, known as shear jamming, has been extensively studied both experimentally [34–37] and numerically [38–41]. Bi *et al.* [33] further proposed the existence of a fragile state in a system under pure shear characterized by the percolation of the force chain only in the compressive direction [42]. In contrast, the force chain in a shear jammed state percolates in all the directions. However, the definition of the fragile state in Ref. [33] is nonquantitative and inapplicable to other systems, necessitating a quantitative definition.

The mutual friction between granular particles results in a distinct rheological transition known as discontinuous shear thickening (DST) [43–63]. DST is important in industrial applications such as protective vests, robotic manipulators, and traction controls [64,65]. Several papers have investigated the relation between DST and shear jamming in suspensions of frictional grains under steady shear [58–61]. In stress-controlled experiments, DST can be observed over a wide region of the phase diagram [58]; however, in rate-controlled experiments, DST can be observed only as a boundary line between shear jamming and continuous shear thickening in the phase diagram [59]. Because these results seem to be inconsistent, the relation between shear jamming and DST is not yet clarified.

To resolve the aforementioned problems, we numerically measure the complex shear modulus in two-dimensional frictional grains near the jamming point under oscillatory shear. Therefore, we apply the discrete element method (DEM) [66]. In Sec. II we explain our setup and model. Section III deals with effects of initial oscillatory shear on the shear modulus. In Sec. IV we clarify the relations among the shear jammed state, the fragile state, and the DST-like behavior by controlling the initial strain amplitude $\gamma_0^{(\mathrm{I})}$ and the area fraction ϕ. We discuss and conclude our results in Sec. V. In Appendix A we explain the details of our simulation. In Appendix B we discuss the dependence of transition points on the friction coefficient μ. The dependence of the phase diagram on the number of the oscillatory shear is discussed in Appendix C. In Appendix D we explain how the shear jammed state appears in the stress-strain curve. In Appendix E we show the fabric anisotropy of the contact network in our simulation.

II. SETUP OF OUR SIMULATION

Let us consider a two-dimensional assembly of *N* frictional granular particles having the identical density ρ confined in
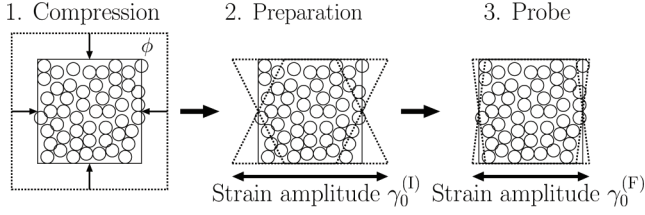
---

*otsuki@me.es.osaka-u.ac.jp

FIG. 1. Illustration of the protocol.

a square box of linear size L. The interparticle interactions are modeled as linear springs with the normal and tangential spring constants of $k^{(n)}$ and $k^{(t)}$, respectively, the friction coefficient μ, and the restitution coefficient e [66]. DEM is detailed in Appendix A. To avoid crystallization, we construct a bidispersed system with an equal number of grains of two diameters (d_0 and $d_0/1.4$). We also adopt $N = 4000$, $k^{(n)} = 0.2k^{(t)}$, $\mu = 1.0$, and $e = 0.043$.

At the beginning of our simulation, the frictional disks are randomly placed with the area fraction $\phi_I = 0.75$, and we slowly compress the system until the area fraction reaches a designated value ϕ as shown in Fig. 1. In each step of the compression process, we increase the area fraction by $\Delta\phi = 10^{-4}$ with the affine transformation, and relax grains to a mechanical equilibrium state where the kinetic temperature $T < T_{th} = 10^{-8}k^{(n)}d_0^2$. We have confirmed that the shear modulus after the compression is insensitive to the choices of T_{th} and $\Delta\phi$ if $T_{th} \leqslant 10^{-8}k^{(n)}d_0^2$ and $\Delta\phi \leqslant 10^{-4}$. Note that we estimate the isotropic jamming point $\phi_{iso} = 0.821$ for $\mu = 1.0$, which might depend on the preparation procedure [67,68]. See Appendix B for the determination and μ dependence of ϕ_{iso}.

We further apply the shear strain

$$\gamma(t) = \gamma_0\{\cos\theta - \cos(\omega t + \theta)\} \qquad (1)$$

in the x direction of the compressed system using the SLLOD method [69] as shown in Fig. 1. Here γ_0, ω, and θ denote the strain amplitude, the angular frequency, and the initial phase, respectively. We apply $N_c^{(I)}$ cycles of the oscillatory shear with the initial strain amplitude $\gamma_0 = \gamma_0^{(I)}$ as a preparation of the system. Note that θ controls the asymmetricity of the applied strain as shown in Fig. 2, where the strain-free state ($\gamma(t) = 0$) is the minimum strain state for $\theta = 0$, while it lies between the maximum and minimum values for $\theta = \pi/2$. After the cycles, we reduce the strain amplitude to $\gamma_0 = \gamma_0^{(F)} = 1.0 \times 10^{-4}$ and apply $N_c^{(F)}$ cycles of the oscillatory shear as a probe to measure
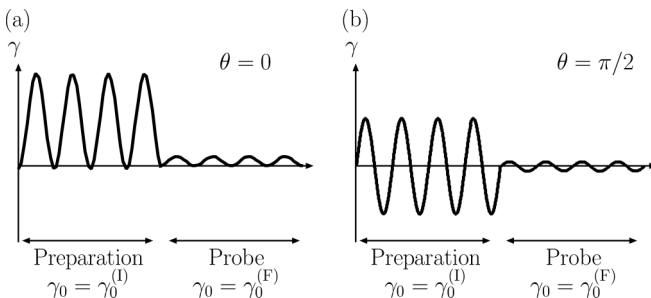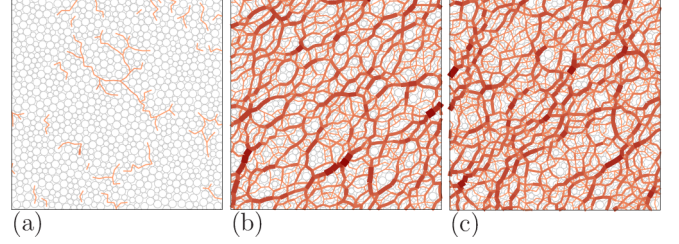

FIG. 2. Plots of the shear strain $\gamma(t)$ against t for $\theta = 0$ (a) and $\pi/2$ (b).

FIG. 3. The snapshots of grains (circles) and force chains (lines) for $\phi = 0.820$ and $\theta = 0$ immediately after the strain amplitudes (a) $\gamma_0^{(I)} = 0.1$, (b) 0.12, and (c) 1.0 are reduced to $\gamma_0^{(F)} = 1.0 \times 10^{-4}$. Panels (a), (b), and (c) correspond to the unjammed, fragile, and shear jammed states, respectively. The color and width of each line depend on the absolute value of the interaction force between grains.

the storage modulus G' and the loss modulus G'' in the linear response region. Here G' and G'' are, respectively, defined by [70]

$$G' = -\frac{\omega}{\pi}\int_0^{2\pi/\omega} dt\, \sigma(t)\cos(\omega t + \theta)/\gamma_0^{(F)}, \qquad (2)$$

$$G'' = \frac{\omega}{\pi}\int_0^{2\pi/\omega} dt\, \sigma(t)\sin(\omega t + \theta)/\gamma_0^{(F)}. \qquad (3)$$

The moduli G' and G'' are measured in the final cycle. The shear stress σ in the above expressions is given by

$$\sigma = -\frac{1}{2L^2}\sum_i\sum_{j>i}(r_{ij,x}F_{ij,y} + r_{ij,y}F_{ij,x}), \qquad (4)$$

where $F_{ij,\alpha}$ and $r_{ij,\alpha}$ denote the α components of the interaction force $\boldsymbol{F}_{ij}$ and the relative position vector $\boldsymbol{r}_{ij}$ between grains i and j, respectively. The contributions of the kinetic part of σ and the coupled stress (i.e., the asymmetric part of the shear stress) are ignored because they are less than 1% of σ. Note that G' and the dynamic viscosity $\eta(\omega) \equiv G''(\omega)/\omega$ corresponding to the apparent viscosity are almost independent of ω and $\gamma_0^{(F)}$ when $\omega \leqslant 10^{-2}t_0^{-1}$, $\gamma_0^{(I)} \leqslant 1.0$, and $\gamma_0^{(F)} \leqslant 10^{-3}$ with $t_0 = \sqrt{m_0/k^{(n)}}$ and the mass m_0 for a grain with the diameter d_0 [71]. Thus, we investigate only the effects of $\gamma_0^{(I)}$, θ, and ϕ on the shear modulus, fixing $\omega = 10^{-4}t_0^{-1}$ and $\gamma_0^{(F)} = 10^{-4}$. We have also confirmed that G' and the phase diagram of the system are almost independent of $N_c^{(I)}$ and $N_c^{(F)}$ when $N_c^{(I)} \geqslant 10$ and $N_c^{(F)} \geqslant 10$ as shown in Appendix C and used $N_c^{(I)} = N_c^{(F)} = 10$. We adopt the leapfrog algorithm with the time step $\Delta t = 0.05t_0$.

III. MECHANICAL RESPONSE

Figure 3 displays the force chains immediately after the reduction of the strain amplitude for $\phi = 0.820 < \phi_{iso}$, and $\theta = 0$ with $\gamma_0^{(I)} = 0.1$, 0.12, and 1.0. When the initial strain amplitude is small ($\gamma_0^{(I)} = 0.1$), the system remains in a liquid-like state with no percolating force chains. Under high initial strains ($\gamma_0^{(I)} = 0.12$ and 1.0), the system develops anisotropic percolating force chains. Unlike the expectation in Ref. [33],
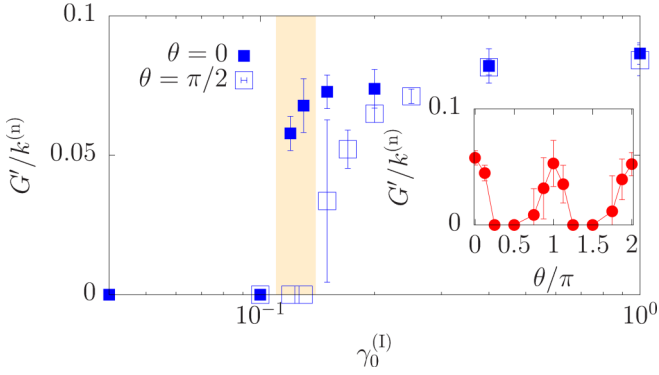
FIG. 4. Plots of the storage modulus G' versus $\gamma_0^{(I)}$ for $\phi = 0.82$ with $\theta = 0$ and $\pi/2$. The shaded region highlights the fragile state. Inset: Storage modulus G' versus θ for $\phi = 0.82$ with $\gamma_0^{(I)} = 0.12$.

the shear jammed state seems to have anisotropic percolating force chains.

Figure 4 displays G' versus $\gamma_0^{(I)}$ for $\theta = 0$ and $\pi/2$ with $\phi = 0.820$. The shear induces transitions from a liquid-like to a solid-like state. See Appendix D for the shear-induced jamming in the stress-strain curve of the initial oscillation. G' strongly depends on θ near the critical strain amplitudes (shaded region of Fig. 4). The inset of Fig. 4 displays G' versus θ for $\phi = 0.82$ and $\gamma_0^{(I)} = 0.12$. The storage modulus G' peaks at $n\pi$ and falls to 0 near $(n + 1/2)\pi$, where n is an integer.

Figure 5 displays the shear stress $\sigma(t)$ versus the strain $\gamma(t)$ in the last cycle of the initial oscillation with $\gamma_0^{(I)} = 1.2$ and $\phi = 0.820$ at $\theta = 0$ and $\pi/2$. When $\theta = 0$, the shear stress σ can be fitted by a linear function of the strain γ near the maximum and minimum values of σ, but remains 0 over $0.03 < \gamma < 0.2$ [Fig. 5(a)]. The linear response near $\gamma \approx 0$ in the stress-strain curve is consistent with the solid-like state after the reduction of the strain amplitude (i.e., $G' > 0$ at $\theta = 0$). Setting $\theta = \pi/2$ shifts the stress-strain curve of the initial oscillation without significantly changing its shape from that of $\theta = 0$ [see Fig. 5(b)]. In this case, the linear response near $\gamma \approx 0$ denotes the liquid-like state after the reduction of the strain amplitude (i.e., $G' = 0$). These results explain the θ dependence of G' in Fig. 4.
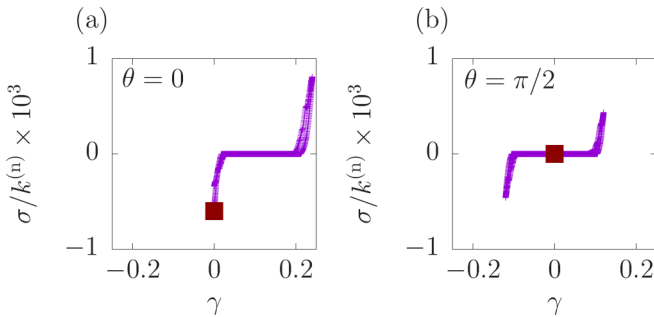

FIG. 5. Plots of the shear stress σ versus the strain γ in the last cycle of the initial oscillatory shear with $\gamma_0^{(I)} = 0.12$ and $\phi = 0.820$ at $\theta = 0$ (a) and $\pi/2$ (b). The solid squares indicate the positions of the linear response measurements after the strain amplitude is reduced.
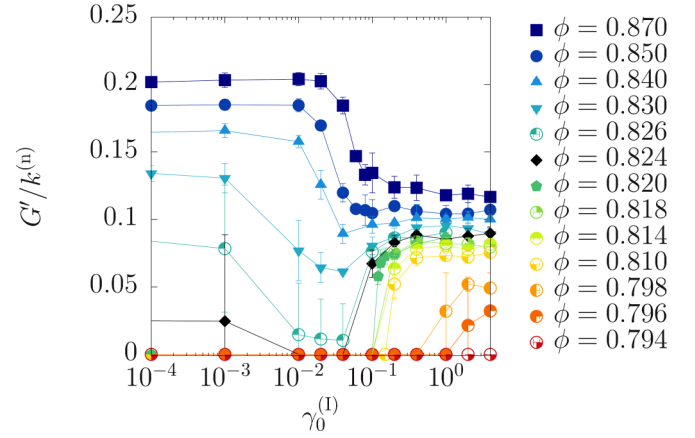

FIG. 6. Plots of the storage modulus G' versus $\gamma_0^{(I)}$ for various ϕ at $\theta = 0$.

Figure 6 displays the storage modulus G' versus $\gamma_0^{(I)}$ for various ϕ at $\theta = 0$. When $\phi > \phi_{\text{iso}} = 0.821$, G' is finite for $\gamma_0^{(I)} = 0$, but depends on $\gamma_0^{(I)}$. When $\phi > 0.84$, G' is a decreasing function of $\gamma_0^{(I)}$, which corresponds to the softening observed in glassy materials under steady-shear conditions [72]. In $0.82 < \phi < 0.84$, G' is minimized at intermediate values of $\gamma_0^{(I)}$. Shear jamming is observed in $\phi_{\text{SJ}} < \phi < \phi_{\text{iso}}$, where $\phi_{\text{SJ}} = 0.795$ (as determined in Appendix B). We also observe a re-entrant behavior at $\phi = 0.824$, where G' changes from $G' > 0$ to $G' \simeq 0$ and reverts to $G' > 0$ at higher $\gamma_0^{(I)}$.

Figure 7 displays the dimensionless dynamic viscosity versus $\gamma_0^{(I)}$ for $\theta = 0$ and various ϕ. The viscosity η is almost independent of $\gamma_0^{(I)}$ when ϕ exceeds ϕ_{iso}, but jumps from a negligibly small value to a large value in $\phi_{\text{SJ}} < \phi < \phi_{\text{iso}}$. This discontinuity, which takes place at a critical amplitude of the initial strain $\gamma_{\text{DST}}^{(I)}$, corresponds to DST under steady shear.

IV. PHASE DIAGRAM

Figure 8 depicts the phase diagram on the $\gamma_0^{(I)}$ versus ϕ plane. Here we have introduced the shear storage modulus without initial oscillatory shear as $G_0'(\phi) \equiv$
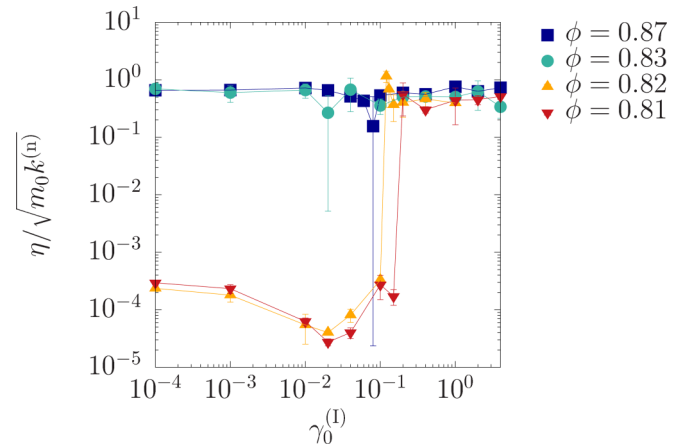

FIG. 7. Plots of the dynamic viscosity η versus the initial strain amplitude $\gamma_0^{(I)}$ for various ϕ at $\theta = 0$.
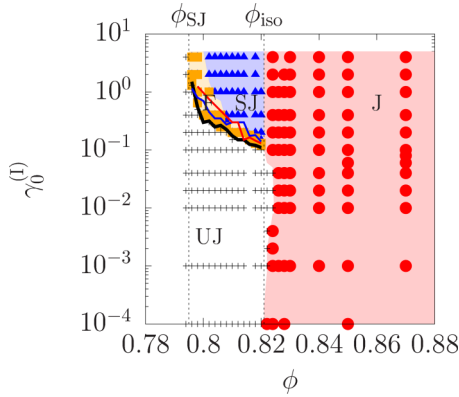
FIG. 8. Phase diagram on the ϕ versus $\gamma_0^{(I)}$ plane. Circles, triangles, squares, and crosses represent the J, SJ, F, and UJ states, respectively. The thick black line, thin blue line, and thin red line represent the critical strain amplitudes $\gamma_{DST}^{(I)}$ at $\theta = 0$, $\pi/4$, and $\pi/2$, respectively.

$\lim_{\gamma_0^{(I)} \to 0} G'(\phi, \gamma_0^{(I)})$. We then define the jammed (J) state in which $G_0'(\phi) > G_{th}$ and $G'(\phi, \gamma_0^{(I)}) > G_{th}$ for any θ with a sufficiently small threshold $G_{th} = 10^{-4} k^{(n)}$. Note that the phase diagram is unchanged by setting $G_{th} = 10^{-5} k^{(n)}$. The unjammed (UJ) state is defined as $G'(\phi, \gamma_0^{(I)}) < G_{th}$ for any θ, and the shear jammed (SJ) state is defined as $G_0'(\phi) < G_{th}$ and $G'(\phi, \gamma_0^{(I)}) > G_{th}$ for any θ. Finally, in the fragile (F) state, whether the state is solid-like with $G'(\phi, \gamma_0^{(I)}) > G_{th}$ or liquid-like with $G'(\phi, \gamma_0^{(I)}) < G_{th}$ depends on the value of θ (see the inset of Fig. 4). In Fig. 8 the SJ state exists in the range $\phi_{SJ} < \phi < \phi_{iso}$ and $\gamma_0^{(I)} > 0.1$. Remarkably, the UJ phase exists even when $\phi > \phi_{iso}$, and the J state at large $\gamma_0^{(I)}$ and $\phi > \phi_{iso}$ (located above the bay-like unjammed state), which is observed in a numerical simulation of frictionless particles under oscillatory shear [73]. This may be regarded as an SJ-like state. However, this state differs from the SJ state defined as the memory effect of the initial strain as introduced above. We have also confirmed the existence of the fragile state between the UJ and SJ states.

Figure 8 also displays the critical strain amplitude $\gamma_{DST}^{(I)}$ for the DST-like behavior, where the viscosity η exceeds a threshold $10^{-3}\sqrt{m_0 k^{(n)}}$. Note that at $\gamma_{DST}^{(I)}$, G' simultaneously changes from 0 to a finite value. When θ is 0, the critical strain amplitude $\gamma_{DST}^{(I)}$ resides on the boundary between the UJ and fragile states, whereas at other θ, it resides in the fragile state. This suggests that the fragile state exhibits the DST-like behavior at least when $\gamma_0^{(I)}$ is not excessively large.

V. DISCUSSION AND CONCLUDING REMARKS

Let us now discuss our results. Recent numerical simulations with different protocols indicated that shear jamming occurs even in frictionless systems [68,74–82]. In our simulation, the SJ state disappears at $\mu = 0$ (see Appendix B). Nevertheless, the re-entrant process in the range $\phi_{iso} < \phi < 0.826$ of our system seems to be related with the SJ states in frictionless systems.

The fragile state was originally defined by the anisotropic percolation of force chains under a quasistatic pure shear
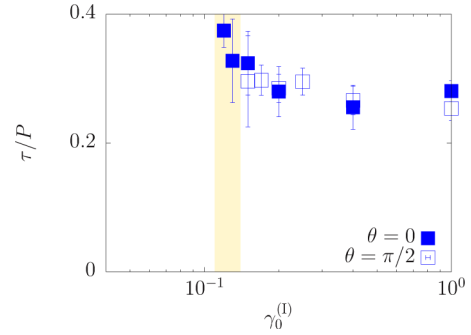

FIG. 9. Plots of the stress anisotropy τ/P versus $\gamma_0^{(I)}$ for $\phi = 0.820$ with $\theta = 0$ and $\pi/2$. The shaded region highlights the fragile state.

process [33]. Because the compressive direction changes with time and no quasistatic operations are imposed in our system, we cannot apply the original argument based on percolation networks [Fig. 3(b)]. Regardless, the stress anisotropy τ/P [39,63,79] immediately after the reduction of the initial strain amplitudes is maximized in the fragile state and remains constant in the SJ state as shown in Fig. 9. In this figure, $\tau = (\sigma_1 - \sigma_2)/2$ and $P = -(\sigma_1 + \sigma_2)/2$, where σ_1 and σ_2 denote the maximum and minimum principal stresses, respectively. This behavior is qualitatively similar to that for the experimentally observed behavior [39] and the fabric anisotropy shown in Appendix E. It is possibly explained by a phenomenology based on the probability distribution of sliding forces [83]. The mutual relation between the fragile state and the anisotropy requires further careful investigation.

In conclusion, we have numerically studied frictional granular systems under oscillatory shearing. By controlling the strain amplitude $\gamma_0^{(I)}$ of the oscillatory shear before measurement, we have observed that a solid-like state with the storage modulus $G' > 0$ is induced. This indicates that shear jamming is an effect of the preparation (cyclic shear), which could be seen as memory effect. We have also observed a fragile state in which the linear response can be solid-like with $G' > 0$ or liquid-like with $G' = 0$ depending on the phase of the oscillation. This protocol has also detected the DST-like behavior, manifesting a remarkable discontinuity in the viscosity versus the initial strain plot. The region of the DST-like behavior in the phase diagram is almost identical with that of the fragile state.

APPENDIX A: DETAILS OF OUR DEM

In this Appendix, we present the details of our DEM. To suppress shear bands, we apply an oscillatory shear along the x direction under Lees-Edwards boundary conditions using the SLLOD method [69]. The equation of motion of grain i (the mass m_i, the position $\boldsymbol{r}_i = (x_i, y_i)$, and the diameter d_i) is written as

$$m_i \frac{d^2}{dt^2} \boldsymbol{r}_i = \boldsymbol{F}_i. \tag{A1}$$

The total force $\boldsymbol{F}_i$ acting on the grain is given by

$$\begin{aligned} \boldsymbol{F}_i &= \sum_{j \neq i} \left(F_{ij}^{(n)} \boldsymbol{n}_{ij} + F_{ij}^{(t)} \boldsymbol{t}_{ij} \right) \\ &= \sum_{j \neq i} \begin{pmatrix} \cos \alpha_{ij} & -\sin \alpha_{ij} \\ \sin \alpha_{ij} & \cos \alpha_{ij} \end{pmatrix} \begin{pmatrix} F_{ij}^{(n)} \\ F_{ij}^{(t)} \end{pmatrix} \end{aligned} \tag{A2}$$

with the normal contact force $F_{ij}^{(n)}$, the tangential contact force $F_{ij}^{(t)}$, the normal unit vector $\boldsymbol{n}_{ij}$, and the tangential unit vector $\boldsymbol{t}_{ij}$ between grains i and j. $\boldsymbol{n}_{ij}$ and $\boldsymbol{t}_{ij}$ respectively, satisfy $\boldsymbol{n}_{ij} = (\cos \alpha_{ij}, \sin \alpha_{ij})$ and $\boldsymbol{t}_{ij} = (-\sin \alpha_{ij}, \cos \alpha_{ij})$ with $\alpha_{ij} = \tan^{-1}[(y_i - y_j)/(x_i - x_j)]$. The normal contact force $F_{ij}^{(n)}$ is given by $F_{ij}^{(n)} = -(k^{(n)} u_{ij}^{(n)} + \zeta^{(n)} v_{ij}^{(n)}) \Theta(d_{ij} - r_{ij})$ with the normal displacement $u_{ij}^{(n)} = r_{ij} - d_{ij}$, $d_{ij} = (d_i + d_j)/2$, $r_{ij} = |\boldsymbol{r}_{ij}| = |\boldsymbol{r}_i - \boldsymbol{r}_j|$, the normal velocity $v_{ij}^{(n)} = (\boldsymbol{v}_i - \boldsymbol{v}_i) \cdot \boldsymbol{n}_{ij}$, the velocity $\boldsymbol{v}_i$ of grain i, the normal spring constant $k^{(n)}$, and the normal damping constant $\zeta^{(n)}$. $\Theta(x)$ is the Heviside step function satisfying $\Theta(x) = 1$ for $x \geqslant 0$ and $\Theta(x) = 0$ otherwise. The tangential force is given by $F_{ij}^{(t)} = \min(|\tilde{F}_{ij}^{(t)}|, \mu F_{ij}^{(n,el)}) \mathrm{sgn}(\tilde{F}_{ij}^{(t)}) \Theta(d_{ij} - r_{ij})$, where μ is the friction coefficient, $\min(a, b)$ selects the smaller one between a and b, $\mathrm{sgn}(x) = 1$ for $x \geqslant 0$ and $\mathrm{sgn}(x) = -1$ otherwise, and $\tilde{F}_{ij}^{(t)}$ is given by $\tilde{F}_{ij}^{(t)} = -k^{(t)} u_{ij}^{(t)} - \zeta^{(t)} v_{ij}^{(t)}$ with the tangential spring constant $k^{(t)}$ and the tangential damping constant $\zeta^{(t)}$. The tangential velocity $v_{ij}^{(t)}$ and the tangential displacement $u_{ij}^{(t)}$, respectively, satisfy $v_{ij}^{(t)} = (\boldsymbol{v}_i - \boldsymbol{v}_i) \cdot \boldsymbol{t}_{ij} - (d_i \omega_i + d_j \omega_j)/2$ and $\dot{u}_{ij}^{(t)} = v_{ij}^{(t)}$ for $|\tilde{F}_{ij}^{(t)}| < \mu F_{ij}^{(n,el)}$ with the angular velocity ω_i of grain i. If $|\tilde{F}_{ij}^{(t)}| \geqslant \mu F_{ij}^{(n,el)}$, $u_{ij}^{(t)}$ remains unchanged. We note that $u_{ij}^{(t)}$ is zero if grains i and j are detached.

We adopt $N = 4000$, $\mu = 1.0$, $k^{(t)} = 0.2 k^{(n)}$, and $\zeta^{(t)} = \zeta^{(n)} = \sqrt{m_0 k^{(n)}}$ in this paper. This set of parameters corresponds to the constant restitution coefficient

$$e = \exp \left(-\frac{\pi}{\sqrt{2 k^{(n)} m_0 / \zeta^{(n)} - 1}} \right) \simeq 0.043 \tag{A3}$$

for a grain with the diameter d_0.

APPENDIX B: DETERMINATION OF TRANSITION POINTS AND THEIR DEPENDENCE ON μ

In this Appendix, we first explain how to determine ϕ_{iso} for the jamming and ϕ_{SJ} for the shear jamming. We also discuss the μ dependence of these transition points.

For a given set of $\gamma_0^{(I)}$ and θ, the storage modulus G' exhibits a transition from $G' = 0$ to $G' > 0$ at a transition
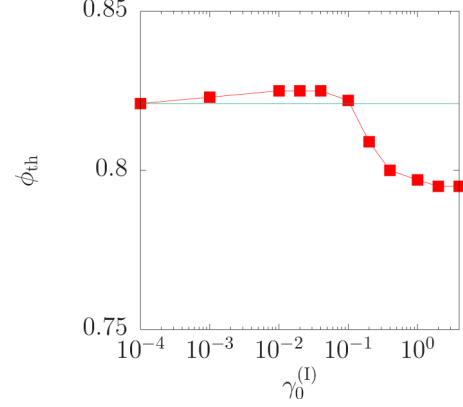

FIG. 10. Plots of the transition point ϕ_{th} versus $\gamma_0^{(I)}$ for $\theta = 0$ and $\mu = 1.0$. The solid thin line parallel to the horizontal axis represents ϕ_{iso}.

point $\phi_{\mathrm{th}}(\gamma_0^{(I)}, \theta)$. In Fig. 10 we plot the transition point $\phi_{\mathrm{th}}(\gamma_0^{(I)}, \theta)$ versus $\gamma_0^{(I)}$ for $\theta = 0$ and $\mu = 1.0$. The transition point increases with $\gamma_0^{(I)}$ for $\gamma_0^{(I)} < 0.04$ and decreases with $\gamma_0^{(I)}$ for $\gamma_0^{(I)} > 0.04$. This dependence of the transition point on the preparation is consistent with the concept of the moving jamming point used to explain the shear jamming in Ref. [68]. Then, we define the jamming point without shear as

$$\phi_{\mathrm{iso}} \equiv \lim_{\gamma_0^{(I)} \to 0} \phi_{\mathrm{th}}(\gamma_0^{(I)}, \theta), \tag{B1}$$

which is independent of θ by definition. It should be noted that ϕ_{iso} is the isotropic jamming point under sufficiently small compression rate without any overcompression used in Ref. [68]. We also define the transition point for the shear jamming as

$$\phi_{\mathrm{SJ}} \equiv \min_{\gamma_0^{(I)}, \theta} \phi_{\mathrm{th}}(\gamma_0^{(I)}, \theta). \tag{B2}$$

Within our observation, $\phi_{\mathrm{th}}(\gamma_0^{(I)}, \theta)$ takes its smallest value at $\theta = 0$ and seems to converge for sufficiently large $\gamma_0^{(I)}$. We, thus, evaluate ϕ_{SJ} as $\phi_{\mathrm{th}}(\gamma_0^{(I)} = 4.0, \theta = 0)$, which is the transition point at the largest initial strain amplitude we apply in our simulation.

In the main text, we have presented the data only for $\mu = 1.0$, but we show the μ dependence of the critical points ϕ_{iso} and ϕ_{SJ} in Fig. 11. Note that the shear jamming in terms of Eq. (B2) is observed only for $\phi_{\mathrm{SJ}} \leqslant \phi \leqslant \phi_{\mathrm{iso}}$. As shown in Fig. 11, the difference between ϕ_{iso} and ϕ_{SJ} decreases as μ decreases. Then, the shear jamming based on our definition disappears in the frictionless limit. This, however, does not deny the shear jamming in frictionless grains in different protocols. Indeed, shear jamming in frictionless grains has been reported in previous studies [68,74–82].

APPENDIX C: THE DEPENDENCE OF THE PHASE BOUNDARIES ON $N_c^{(I)}$

In this section, we show the dependence of the phase diagram on the number $N_c^{(I)}$ of cycles in the initial oscillatory shear. Here we introduce the minimum strain amplitude $\gamma_{0,\mathrm{min}}^{(I)}(\phi)$ for SJ, where $G'(\phi, \gamma_0^{(I)}) > G_{\mathrm{th}}$ for any θ if $\gamma_0^{(I)} >$
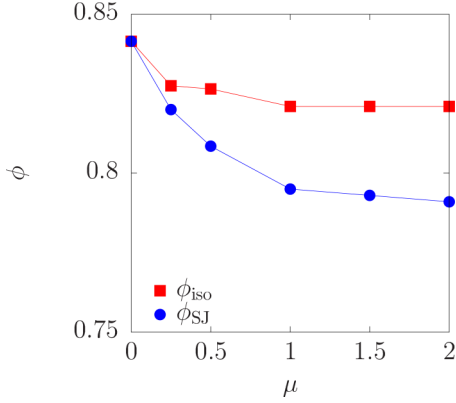
FIG. 11. Plots of the transition points $\phi_{\rm iso}$ and $\phi_{\rm SJ}$ versus μ.

$\gamma_{0,\min}^{({\rm I})}(\phi)$. It should be noted that $\gamma_{0,\min}^{({\rm I})}(\phi)$ gives the boundary between the SJ and F states in Fig. 8. In Fig. 12 we plot $\gamma_{0,\min}^{({\rm I})}(\phi)$ versus ϕ for various $N_c^{({\rm I})}$, where $\gamma_{0,\min}^{({\rm I})}(\phi = 0.82)$ slightly increase with $N_c^{({\rm I})}$, though $\gamma_{0,\min}^{({\rm I})}(\phi)$ is insensitive to $N_c^{({\rm I})}$ for $\phi \leqslant 0.81$. Therefore, we safely state that $\gamma_{0,\min}^{({\rm I})}(\phi)$ converges for $N_c^{({\rm I})} \geqslant 10$ and arbitrary ϕ.

APPENDIX D: INITIAL STRESS-STRAIN CURVE AND THE SHEAR JAMMING

In this Appendix, we explain how the shear jamming in the linear response regime is related to the initial stress-strain curve for large strain amplitudes. We also explain the reason why the liquid-like response can be observed if the initial strain amplitude is sufficiently small.

In Fig. 13 we plot the shear stress σ versus the strain γ for $\gamma_0^{({\rm I})} = 0.2$, $\phi = 0.820$, and $\theta = 0$. Note that $\gamma_0^{({\rm I})} = 0.2$ for this area fraction corresponds to the shear jammed state. The stress σ follows a stress-strain loop once γ exceeds $\gamma \simeq 0.02$. Even after the reduction of the strain amplitude, there is finite gradient of σ against γ around $\gamma = 0$, which is equivalent to $G' > 0$. Note that the red filled square in Fig. 13 is the measurement point. This emergence of $G' > 0$ is regarded as the occurrence of the shear jamming.

Figure 13 is useful to understand the reason why we observe the liquid-like response if $\gamma_0^{({\rm I})}$ is small for $\phi = 0.82$ and $\theta = 0$. Indeed, σ remains almost zero for $\gamma \leqslant 0.01$ in this
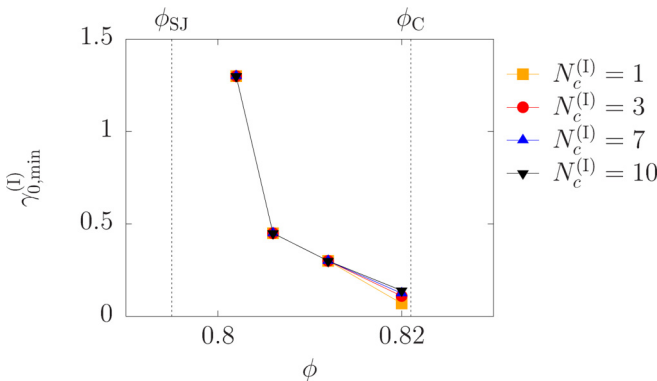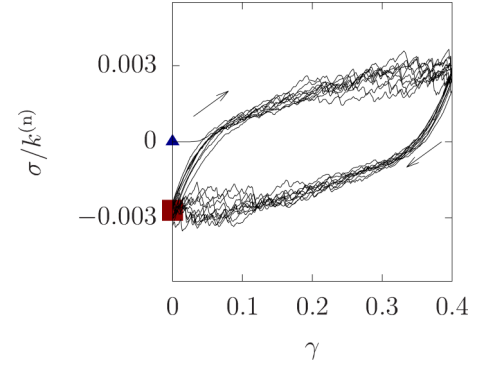

FIG. 13. Plots of the shear stress σ versus the strain γ for $\gamma_0^{({\rm I})} = 0.2$, $\phi = 0.820$, and $\theta = 0$. The triangle and the square indicate the states before and after the initial oscillatory shear, respectively. The arrows indicate the direction of time evolution in the stress-strain curve.

figure. Then, if we reduce γ_0 to $\gamma_0^{({\rm F})} = 1.0 \times 10^{-4}$, we obtain only $G' = 0$ for $\gamma_0^{({\rm I})} \leqslant 0.01$.

APPENDIX E: FABRIC ANISOTROPY OF CONTACT NETWORK

In this Appendix, we present the result of the fabric anisotropy of the contact network in the fragile and shear jammed states. Let us introduce the contact fabric tensor $R_{\alpha\beta}$ as [33]

$$R_{\alpha\beta} = \frac{1}{N} \sum_i \sum_{j>i} \frac{r_{ij,\alpha} r_{ij,\beta}}{r_{ij}^2} \Theta(d_{ij} - r_{ij}). \qquad ({\rm E1})$$

Figure 14 displays the fabric anisotropy $R_1 - R_2$ versus $\gamma_0^{({\rm I})}$ for $\phi = 0.820$ with $\theta = 0$ and $\pi/2$, where the maximum and the minimum eigenvalues of $R_{\alpha\beta}$ are denoted as R_1 and R_2, respectively. The fabric anisotropy takes the maximum in the fragile state and keeps constant in SJ, which corresponds to the stress anisotropy in Fig. 9.

FIG. 12. Plots of $\gamma_{0,\min}^{({\rm I})}(\phi)$ versus ϕ for various $N_c^{({\rm I})}$.
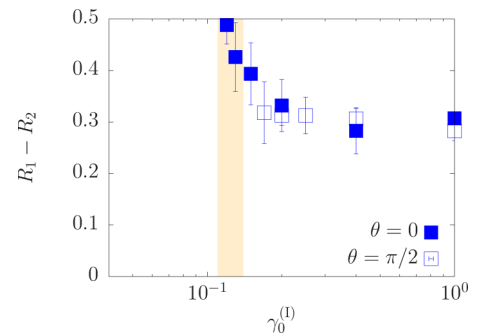

FIG. 14. Plots of the fabric anisotropy $R_1 - R_2$ versus $\gamma_0^{({\rm I})}$ for $\phi = 0.820$ with $\theta = 0$ and $\pi/2$. The shaded region corresponds to the fragile state.

[1] A. J. Liu and S. R. Nagel, Nature (London) **396**, 21 (1998).

[2] M. van Hecke, J. Phys.: Condens. Matter **22**, 033101 (2009)

[3] R. P. Behringer and B. Chakraborty, Rep. Prog. Phys. **82**, 012601 (2018).

[4] C. S. O'Hern, S. A. Langer, A. J. Liu, and S. R. Nagel, Phys. Rev. Lett. **88**, 075507 (2002).

[5] C. S. O'Hern, L. E. Silbert, A. J. Liu, and S. R. Nagel, Phys. Rev. E **68**, 011306 (2003).

[6] M. Wyart, Ann. Phys. Fr. **30**, 3 (2005).

[7] P. Olsson and S. Teitel, Phys. Rev. Lett. **99**, 178001 (2007).

[8] T. Hatano, M. Otsuki, and S. Sasa, J. Phys. Soc. Jpn. **76**, 023001 (2007).

[9] T. Hatano, J. Phys. Soc. Jpn. **77**, 123002 (2008).

[10] B. P. Tighe, E. Woldhuis, J. J. C. Remmers, W. van Saarloos, and M. van Hecke, Phys. Rev. Lett. **105**, 088303 (2010).

[11] T. Hatano, Prog. Theor. Phys. Suppl. **184**, 143 (2010).

[12] M. Otsuki and H. Hayakawa, Prog. Theor. Phys. **121**, 647 (2009).

[13] M. Otsuki and H. Hayakawa, Phys. Rev. E **80**, 011308 (2009).

[14] M. Otsuki, H. Hayakawa, and S. Luding, Prog. Theor. Phys. Suppl. **184**, 110 (2010).

[15] K. N. Nordstrom, E. Verneuil, P. E. Arratia, A. Basu, Z. Zhang, A. G. Yodh, J. P. Gollub, and D. J. Durian, Phys. Rev. Lett. **105**, 175701 (2010).

[16] P. Olsson and S. Teitel, Phys. Rev. E **83**, 030302(R) (2011).

[17] D. Vågberg, P. Olsson, and S. Teitel, Phys. Rev. E **83**, 031307 (2011).

[18] M. Otsuki and H. Hayakawa, Prog. Theor. Phys. Suppl. **195**, 129 (2012).

[19] A. Ikeda, L. Berthier, and P. Sollich, Phys. Rev. Lett. **109**, 018301 (2012).

[20] P. Olsson and S. Teitel, Phys. Rev. Lett. **109**, 108001 (2012).

[21] E. DeGiuli, G. Düring, E. Lerner, and M. Wyart, Phys. Rev. E **91**, 062206 (2015).

[22] D. Vågberg, P. Olsson, and S. Teitel, Phys. Rev. E **93**, 052902 (2016).

[23] F. Boyer, E. Guazzelli, and O. Pouliquen, Phys. Rev. Lett. **107**, 188301 (2011).

[24] M. Trulsson, B. Andreotti, and P. Claudin, Phys. Rev. Lett. **109**, 118305 (2012).

[25] B. Andreotti, J.-L. Barrat, and C. Heussinger, Phys. Rev. Lett. **109**, 105901 (2012).

[26] E. Lerner, G. Düring, and M. Wyart, Proc. Natl. Acad. Sci. USA **109**, 4798 (2012).

[27] D. Vågberg, P. Olsson, and S. Teitel, Phys. Rev. Lett. **113**, 148002 (2014).

[28] T. Kawasaki, D. Coslovich, A. Ikeda, and L. Berthier, Phys. Rev. E **91**, 012203 (2015).

[29] K. Suzuki and H. Hayakawa, Phys. Rev. Lett. **115**, 098001 (2015).

[30] S. H. E. Rahbari, J. Vollmer, and H. Park, Phys. Rev. E **98**, 052905 (2018).

[31] B. P. Tighe, Phys. Rev. Lett. **107**, 158303 (2011).

[32] M. Otsuki and H. Hayakawa, Phys. Rev. E **90**, 042202 (2014).

[33] D. Bi, J. Zhang, B. Chakraborty, and R. Behringer, Nature (London) **480**, 355 (2011).

[34] J. Zhang, T. Majmudar, and R. Behringer, Chaos **18**, 041107 (2008).

[35] J. Zhang, T. S. Majmudar, A. Tordesillas, and R. P. Behringer, Granular Matter **12**, 159 (2010).

[36] D. Wang, J. Ren, J. A. Dijksman, H. Zheng, and R. P. Behringer, Phys. Rev. Lett. **120**, 208004 (2018).

[37] Y. Zhao, J. Barés, H. Zheng, J. E. S. Socolar, and R. P. Behringer, Phys. Rev. Lett. **123**, 158001 (2019).

[38] S. Sarkar, D. Bi, J. Zhang, R. P. Behringer, and B. Chakraborty, Phys. Rev. Lett. **111**, 068301 (2013).

[39] S. Sarkar, D. Bi, J. Zhang, J. Ren, R. P. Behringer, and B. Chakraborty, Phys. Rev. E **93**, 042901 (2016).

[40] R. Seto, A. Singh, B. Chakraborty, M. M. Denn, and J. F. Morris, Granular Matter **21**, 82 (2019).

[41] Pradipto and H. Hayakawa, Soft Matter **16**, 945 (2020).

[42] In Ref. [33] the force chains consist of particles connected via interaction forces larger than their average.

[43] M. Otsuki and H. Hayakawa, Phys. Rev. E **83**, 051301 (2011).

[44] S. Chialvo, J. Sun, and S. Sundaresan, Phys. Rev. E **85**, 021305 (2012).

[45] E. Brown and H. M. Jaeger, Phys. Rev. Lett. **103**, 086001 (2009).

[46] R. Seto, R. Mari, J. F. Morris, and M. M. Denn, Phys. Rev. Lett. **111**, 218301 (2013).

[47] N. Fernandez, R. Mani, D. Rinaldi, D. Kadau, M. Mosquet, H. Lombois-Burger, J. Cayer-Barrioz, H. J. Herrmann, N. D. Spencer, and L. Isa, Phys. Rev. Lett. **111**, 108301 (2013).

[48] C. Heussinger, Phys. Rev. E **88**, 050201(R) (2013).

[49] M. M. Bandi, M. K. Rivera, F. Krzakala, and R. E. Ecke, Phys. Rev. E **87**, 042205 (2013).

[50] M. P. Ciamarra, R. Pastore, M. Nicodemi, and A. Coniglio, Phys. Rev. E **84**, 041308 (2011).

[51] R. Mari, R. Seto, J. F. Morris, and M. M. Denn, J. Rheol. **58**, 1693 (2014).

[52] M. Grob, C. Heussinger, and A. Zippelius, Phys. Rev. E **89**, 050201(R) (2014).

[53] T. Kawasaki, A. Ikeda, and L. Berthier, Europhys. Lett. **107**, 28009 (2014).

[54] M. Wyart and M. E. Cates, Phys. Rev. Lett. **112**, 098302 (2014).

[55] M. Grob, A. Zippelius, and C. Heussinger, Phys. Rev. E **93**, 030901(R) (2016).

[56] H. Hayakawa and S. Takada, Prog. Theor. Exp. Phys. **2019**, 083J01 (2019).

[57] H. Hayakawa, S. Takada, and V. Garzo, Phys. Rev. E **96**, 042903 (2017).

[58] I. R. Peters, S. Majumdar, and H. M. Jaeger, Nature (London) **532**, 214 (2016).

[59] A. Fall, F. Bertrand, D. Hautemayou, C. Mezière, P. Moucheront, A. Lemaître, and G. Ovarlez, Phys. Rev. Lett. **114**, 098301 (2015).

[60] S. Sarkar, E. Shatoff, K. Ramola, R. Mari, J. Morris, and B. Chakraborty, EPJ Web Conf. **140**, 09045 (2017).

[61] A. Singh, R. Mari, M. M. Denn, and J. F. Morris, J. Rheol. **62**, 457 (2018).

[62] T. Kawasaki and L. Berthier, Phys. Rev. E **98**, 012609 (2018).

[63] J. E. Thomas, K. Ramola, A. Singh, R. Mari, J. F. Morris, and B. Chakraborty, Phys. Rev. Lett. **121**, 128002 (2018).

[64] E. Brown and H. M. Jaeger, Rep. Prog. Phys. **77**, 046602 (2014).

[65] E. Brown, N. Rodenberg, J. Amend, A. Mozeika, E. Steltz, M. R. Zakin, H. Lipson, and H. M. Jaeger, Proc. Natl. Acad. Sci. USA **107**, 18809 (2010).

[66] P. A. Cundall and O. D. L. Strack, Geotechnique **29**, 47 (1979).

[67] S. Luding, Nat. Phys. **12**, 531 (2016).

[68] N. Kumar and S. Luding, Granular Matter **18**, 58 (2016).

[69] D. J. Evans and G. P. Morriss, *Statistical Mechanics of Nonequilibrium Liquids*, 2nd ed. (Cambridge University Press, Cambridge, 2008).

[70] M. Doi and S. F. Edwards, *The Theory of Polymer Dynamics* (Oxford University Press, Oxford, 1986).

[71] M. Otsuki and H. Hayakawa, Phys. Rev. E **95**, 062902 (2017).

[72] M. Fan, K. Zhang, J. Schroers, M. D. Shattuck, and C. S. O'Hern, Phys. Rev. E **96**, 032602 (2017).

[73] P. Das, H. A. Vinutha, and S. Sastry, arXiv:1907.08503.

[74] Y. Jin and H. Yoshino, Nat. Commun. **8**, 14935 (2017).

[75] P. Urbani and F. Zamponi, Phys. Rev. Lett. **118**, 038001 (2017).

[76] Y. Jin, P. Urbani, F. Zamponi, and H. Yoshino, Sci. Adv. **4**, eaat6387 (2018)

[77] T. Bertrand, R. P. Behringer, B. Chakraborty, C. S. O'Hern, and M. D. Shattuck, Phys. Rev. E **93**, 012901 (2016).

[78] M. Baity-Jesi, C. P. Goodrich, A. J. Liu, S. R. Nagel, and J. P. Sethna, J. Stat. Phys. **167**, 735 (2017).

[79] S. Chen, T. Bertrand, W. Jin, M. D. Shattuck, and C. S. O'Hern, Phys. Rev. E **98**, 042906 (2018).

[80] H. A. Vinutha and S. Sastry, Nat. Phys. **12**, 578 (2016).

[81] H. A. Vinutha and S. Sastry, J. Stat. Mech. (2016) 094002.

[82] H. A. Vinutha and S. Sastry, Phys. Rev. E **99**, 012123 (2019).

[83] E. DeGiuli and M. Wyart, Proc. Natl. Acad. Sci. USA **114**, 9284 (2017).